arXiv:1109.3478v1 [astro-ph.GA] 15 Sep 2011

Flaws in the perfect bubble

S. Walch[1]
stefanie.walch@astro.cf.ac.uk

A. Whitworth[1]

T. Bisbas[2]

D. A. Hubber[3,4]

R. Wünsch[5]

ABSTRACT

Perfect bubbles like that surrounding the galactic HII region RCW 120 (Deharveng et al. 2009) have been interpreted as proof of concept for the collect and collapse (C&C) mechanism of triggered star formation. The cold, dusty clumps surrounding RCW 120 are aligned along an almost spherical shell. It has been inferred that these massive clumps, which sometimes harbour young stellar objects, have been formed via the fragmentation of the dense, swept-up shell. In order to better understand the triggering mechanisms at work in shells like RCW 120, we perform high-resolution, three dimensional SPH simulations of HII regions expanding into fractal molecular clouds. In a second step, we use RADMC-3D to compute the synthetic dust continuum emission from our simulations, in order to compare them with observations of RCW 120 made with APEX-LABOCA at 870 μm. We show that a distribution of clumps similar to the one seen in RCW 120 can readily be explained by a non-uniform underlying molecular cloud structure. Hence, a shell-like clump configuration around an HII region does not necessarily support the C&C scenario, but rather reflects the pre-existing, non-uniform density distribution of the molecular cloud into which the HII region expands.

Subject headings: ISM: bubbles - HII regions - ISM: structure - stars: formation - radiative transfer

1. Introduction

The possibility of triggering star formation by ionizing feedback from young, massive stars has been explored for several decades. From a theoretical point of view, two main triggering mechanisms have been suggested: Collect and Collapse (C&C), and Radiation Driven Implosion (RDI).

The C&C mechanism was first analyzed by Elmegreen & Lada (1977). In this mechanism the expanding HII region sweeps up a layer of cold gas and dust beyond the ionization front (e.g.

---

[1] School of Physics and Astronomy, Cardiff University, Queens Buildings, 5 The Parade, CF24 3AA, Cardiff, UK

[2] Department of Physics & Astronomy, University College London, London WC1E 6BT, UK

[3] Department of Physics & Astronomy, University of Sheffield, Sheffield S3 7RH, UK

[4] School of Physics and Astronomy, University of Leeds, Leeds, LS2 9JT, UK

[5] Astronomical Institute, Academy of Sciences of the Czech Republic, Bocni II 1401, 141 31 Prague, Czech Republic

Dale et al. 2007), and this shell eventually becomes gravitationally unstable due to the growth of perturbations along its surface (Elmegreen 1994; Whitworth et al. 1994a; Dale et al. 2009; Wünsch et al. 2010). One argument in favour of the C&C mechanism is that it is predicted to spawn massive fragments (Whitworth et al. 1994b), and hence it affords the possibility of forming massive stars sequentially.

In contrast, RDI (Kessel-Deynet & Burkert 2003; Sandford et al. 1982; Bisbas et al. 2011) triggers star formation by compressing pre-existing cold, but otherwise gravitationally stable, molecular cloud cores. Previous observational and theoretical studies (e.g. Gritschneder et al. 2009, 2010) suggest that RDI leads to star formation in the tips of pillar-like structures, for example as seen in the Eagle nebula (White et al. 1999). Bisbas et al. (2011) have published a detailed numerical study of RDI in initially stable Bonnor-Ebert spheres.

The nearby HII region RCW 120 is one of the most studied HII regions in the Galactic plane. As observed with Spitzer at 8 μm (Churchwell et al. 2006), it appears to be an almost perfectly round bubble with a well defined ionization front. Zavagno et al. (2007) and Deharveng et al. (2009) have combined Spitzer and 2MASS data with observations at 870μm and 1.2mm, to analyze the star formation associated with RCW 120. They infer that this star formation has been triggered by the C&C mechanism. Similar conclusions have been drawn for other regions, e.g. Sh 104 (Deharveng et al. 2003) and RCW 79 (Zavagno et al. 2006), where the C&C scenario is preferred due to the existence of very massive cold clumps. Performing radiation-magnetohydrodynamic simulations of HII regions, Arthur et al. (2011) point out that bubble structures like RCW 120 should be quite common. However, their simulations do not include self-gravity and therefore conclusions on shell fragmentation, clump formation and triggered star formation could not be drawn.

In this paper we show that a distribution of massive clumps around an HII region can be explained without invoking the C&C mechanism, if the HII region expands into a non-uniform medium. This scenario does not require a shell to be collected and then fragment. Indeed, we find that the C&C mechanism is only viable if the cloud into which the HII region expands is extremely uniform, which seems very unlikely. Observed clumpy, shell-like structures like that seen in RCW 120 are most likely the consequence of pre-existing structures in the natal molecular cloud.

The plan of this paper is the following. In section 2 we describe the algorithm used to generate initial fractal molecular clouds, and the numerical method used to evolve them, including the treatment of ionizing radiation. In section 3 we describe the resulting HII regions and the modeled synthetic 870μm observations. We discuss the shell and clump masses inferred from the synthetic observations in section 4, and compare them with the true masses. Our main conclusions are summarized in section 5.

2. Initial conditions & numerical method

2.1. The generation of a fractal molecular cloud

The initial three-dimensional fractal density structure is constructed using an FFT-based algorithm. The algorithm has three main input parameters, (i) the 3D power spectral index n, where $P(k) \propto k^n$, (ii) the random seed $\mathcal{R}$ used to generate a particular cloud realisation, and (iii) the density scaling constant ρ_0 (see below). We populate the integer modes $k = 1, .., 128$ along each Cartesian axis (x, y, z), where $k = 1$ corresponds to the linear box size in one dimension. According to Stutzki et al. (1998), the fractal box-coverage dimension, D, of a fractal structure embedded in three-dimensional space is related to the power spectrum by

$$\mathcal{D} = 3 - \frac{(n-2)}{2} \qquad (1)$$

(see also Federrath et al. 2009). Thus, defining $\mathcal{D}$ is equivalent to defining the power spectral index n. Here, we choose setups with $\mathcal{D} = 2.4$, in agreement with observations of molecular clouds in the Milky Way (Falgarone et al. 1991; Vogelaar & Wakker 1994; Stutzki et al. 1998; Lee 2004; Sánchez et al. 2005). This corresponds to $n = 3.2$.

After constructing the density fluctuations in Fourier space and applying the FFT to give $\rho_{\rm FFT}(x, y, z)$ on a 128^3 grid, the resulting field is scaled using an exponential:

$$\rho(x,y,z) = \exp\left(\frac{\rho_{\rm FFT}}{\rho_0}\right), \qquad (2)$$

where ρ_0 is an arbitrary scaling constant. The resulting density field has log-normal density probability density function (PDF) and a clump mass distribution in agreement with observations (as described in Shadmehri & Elmegreen 2011). In particular, for a given spectrum of density fluctuations, changing ρ_0 allows us to adjust the width of the density PDF, i.e. the variance σ of the log-normal distribution, whilst leaving the underlying topology of the density field unchanged. In Figure 1 we show the resulting density PDFs for setups having equal fractal dimension $\mathcal{D} = 2.4$ and the same random seed $\mathcal{R}$, but two different values of ρ_0.

2.2. Initial conditions

We choose a cloud with total mass of $\rm M_{MC} = 10^4\ M_\odot$, and radius of $R_{\rm MC} = 5.0$ pc. This results in a mean density of $\bar{\rho} = 5.42\times10^{-21}{\rm g\ cm^{-3}}$, or equivalently $\bar{n} = 1380\ {\rm cm^{-3}}$ for molecular gas having mean molecular weight $\mu = 2.35$. In this paper, we discuss two simulations, both of which result in a shell-like structure very similar to the one observed in RCW 120. Apart from the scaling parameter ρ_0, the initial clouds are identical, i.e. their density fields have the same topological structure. The simulation with $\rho_0 = 1.5$ is called *Run 1*, and the simulation with $\rho_0 = 1.0$ is called *Run 2*. By fitting their density PDFs using a χ-squared minimisation method, we estimate the corresponding logarithmic density variances, viz. $\sigma_1 = 0.88$ (*Run 1*), and $\sigma_2 = 1.31$ (*Run 2*).

We can relate σ to the conditions produced in turbulent gas by introducing the scaling relation between the width of the density PDF and the turbulent Mach number derived by Padoan et al. (1997), Padoan & Nordlund (2002) and Federrath et al. (2008),

$$\sigma^2 = \ln\left(1 + {\rm b}^2{\rm M}^2\right)\ , \qquad (3)$$

with $b \simeq 0.5$. According to this relation, the density field in *Run 1* corresponds to a molecular cloud with Mach 2.2 turbulence; and *Run 2* corresponds to Mach 4.3 turbulence.

Before populating the computational box with SPH particles, we shift the point of maximum density to the center of the computational domain, and position the ionizing star there. Then we cut out a sphere with radius $R_{\rm MC}$, centered on the ionizing star. Finally, we partition the computational box with a 128^3 grid, compute the mass in each cell of the grid, and apportion each cell the corresponding number of SPH particles, distributed randomly within the cell.

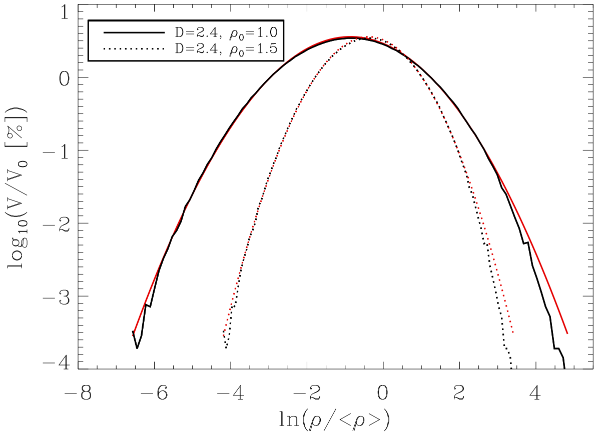

Fig. 1.— Density PDFs derived for fractal cloud having the same fractal dimension $\mathcal{D} = 2.4$ and random seed $\mathcal{R}$, but different density scaling parameters $\rho_0 = 1.0$ and $\rho_0 = 1.5$ (black lines). Both distributions have been fitted with a log-normal (red lines).

2.3. Numerical method: SPH

We use the SPH code SEREN (Hubber et al. 2011a), which is well-tested and has already been applied to many problems in star formation (e.g. Walch et al. 2011; Bisbas et al. 2011; Stamatellos et al. 2011). The ionizing radiation is treated with a HEALPix-based adaptive ray-splitting algorithm, which allows for optimal resolution of the ionization front in high resolution simulations (see Bisbas et al. 2009). We employ the standard SPH algorithm (Monaghan 1992). The SPH equations of motion are solved with a second-order Leapfrog integrator, in conjunction with a block time-stepping scheme. Gravitational forces are calculated using an octal spatial decomposition tree (Barnes & Hut 1986), with monopole and quadrupole terms and a Gadget-style opening-angle criterion (Springel et al. 2001). We use the standard artificial viscosity prescription (Monaghan & Gingold 1983), moderated with a Balsara switch (Balsara 1995).

The temperature of ionized gas particles is set to 10,000 K. The temperature of neutral gas is given by a barotropic equation of state,

$$T(\rho) = T_{\rm MIN}\left[1 + (\rho/\rho_{\rm CRIT})^{(\gamma-1)}\right], \qquad (4)$$

where the isothermal temperature is $T_{\rm MIN} = 30\,{\rm K}$, the critical density is $\rho_{\rm CRIT} = 10^{-13}\,{\rm g\,cm^{-3}}$, and the adiabatic index is $\gamma = 5/3$. The use of $T_{\rm MIN} = 30\,{\rm K}$ might influence the fragmentation properties of the forming shell. Since the shell becomes very dense and should therefore be allowed to cool further, it might fragment more efficiently than currently seen in our simulations. For this reason will explore a more complicated cooling function in a future paper.

We introduce sinks at density peaks above $\rho_{\rm SINK} = 10^{-11}\,{\rm g\,cm^{-3}}$, provided that the density peak in question is at the bottom of its local gravitational potential well (see Hubber et al. 2011b, in prep.). Since $\rho_{\rm SINK} \gg \rho_{\rm CRIT}$, a condensation that is translated into a sink is always well into its Kelvin-Helmholtz contraction phase. Once formed, a sink is able to accrete gas smoothly from its surroundings (see Hubber et al. 2011b, in prep.) and thereby grow in mass. Sinks are identified as protostars, and their radiation can be included in the radiative transfer models produced with RADMC-3D in the post-processing step (see section 3.3).

3. Results

3.1. SPH simulations

In this subsection we discuss the results of the SPH simulations. In both *Run 1* and *Run 2* a source of ionizing radiation emitting $\dot{N}_{\rm LyC} = 10^{49}\,{\rm s^{-1}}$ is placed at the center of the cloud. This corresponds approximately to an O7.5 ZAMS star with a mass of $\sim 25{\rm M_\odot}$ and a surface temperature of $\sim 40,000\,{\rm K}$ (Osterbrock & Ferland 2006, Table 2.3). Thus, the used central source is slightly stronger than the central star within RCW 120, which is estimated to be a O8.5 - O9 star emitting $\dot{N}_{\rm LyC} = 10^{48.04\pm0.1}\ {\rm s^{-1}}$ (Zavagno et al. 2007).

In both simulations we use 2.5×10^6 SPH particles. Thus, each particle has a mass $m_{\rm part} = 4.0 \times 10^{-3}\ {\rm M_\odot}$ and the minimum resolvable mass is $\sim 0.4\ {\rm M_\odot}$.

In Figure 2, we show the initial and final column density distributions for the simulations. Note that *Run 2* has the broader density PDF, and hence the more pronounced density contrasts in the initial conditions. Both setups develop an HII region with a diameter of $\sim$ 5 pc. We compare the two simulations at the time when a total mass of $\sim 500\ {\rm M_\odot}$ has been converted into stars, which is $t_{\rm END} = 0.98$ Myr for *Run 1* and $t_{\rm END} = 0.68$ Myr for *Run 2*. [1] The black dots in the evolved HII regions mark sinks, i.e. protostars. At $t_{\rm END}$ there are 79 sinks in *Run 1* and 38 sinks in *Run 2*. We stress that the simulations are highly dynamical. New protostars are constantly formed and existing protostars continue to accrete at different rates. In Figure 3, we plot the mass accretion rate onto each protostar as a function of its mass. The accretion rates of protostars that have essentially stopped accreting are arbitrarily set to $\dot{\rm M}_{\rm MIN} = 10^{-10}\ {\rm M_\odot yr^{-1}}$. For all other sinks there is no clear correlation between sink mass and mass accretion rate, and we find a mean accretion rate of about $10^{-5}\ {\rm M_\odot yr^{-1}}$ in both simulations. *Run 2* forms more massive stars than *Run 1*.

3.2. Overall bubble structure

As with RCW 120, we find that the shells formed in our simulations are not perfectly spherically symmetric, but elongated and perforated. For example, in the simulations illustrated in Fig. 2 the initial cloud has a region of reduced column density in the northwest corner, where the ionized gas is able to stream out of the HII region and open a hole in the shell.

Deharveng et al. (2009) note the presence of radially oriented, filamentary streams below the dense, southern part of the shell in RCW 120, and suggest that these filaments are due to the pressure exerted by the ionized gas. Our simulations suggest an alternative mechanism for the formation of such filaments. As shown in the bottom

---

[1] Both runs could be followed further, but become extremely time-consuming and slow once the dense shell is collapsing in many places.

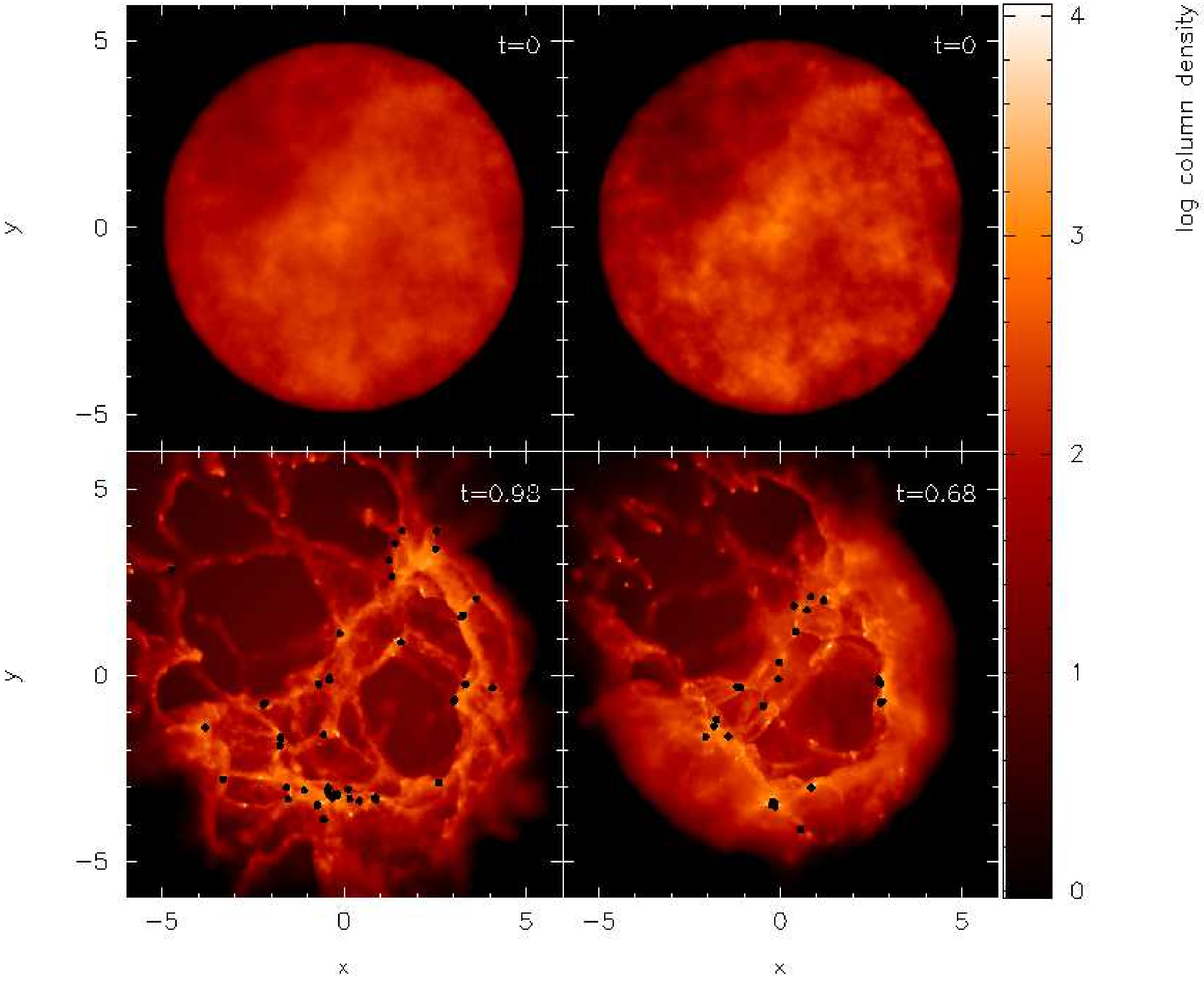

Fig. 2.— *Upper panels:* Initial column density distribution in [$M_\odot$ pc^{-2}] for two representative fractal clouds. Both initial conditions were derived with a fractal dimension of $\mathcal{D} = 2.4$ and the same random seed $\mathcal{R}$, but different scaling densities $\rho_0 = 1.5$ (Run 1; left column) and $\rho_0 = 1.0$ (Run 2; right column). *Lower panels:* The column density distributions at $t_{\rm END}$ after an HII region has formed and part of the molecular cloud has been swept up into a shell. The black dots mark sink particles, i.e. forming protostars.

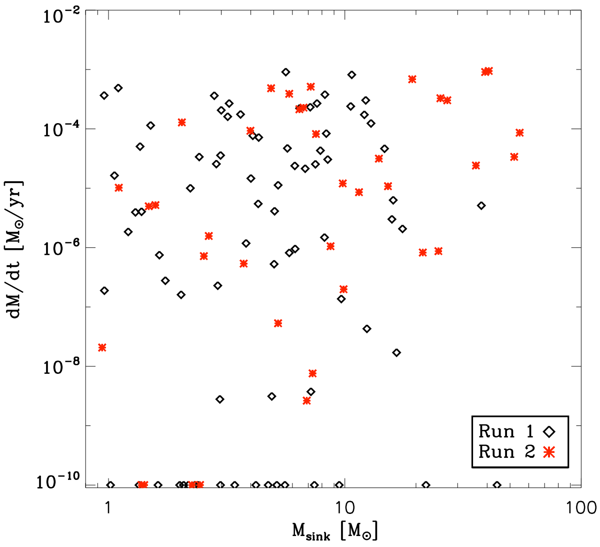

Fig. 3.— Mass accretion rate vs. current sink mass for *Run 1* and *Run 2* at $t_{\rm END}$.

Run 1			*Run 2*		
C	$M_{\rm SINK,tot}$ [M$_\odot$]	$N_{\rm SINK}$	C	$M_{\rm SINK,tot}$ [M$_\odot$]	$N_{\rm SINK}$
Shell	400.	31	Shell	483.	36
C1	0.0	0	C1	34.6	3
C2	0.0	0	C2	54.2	6
C3	140.	11	C3	171.	9

Table 1: Properties of the protostars embedded in the shell and the main clumps. Column 1 gives the ID of the clump. Columns 2 and 3 give the total mass and total number of protostars embedded within the clumps at $t_{\rm END}$. Note that the sink masses do not add up to the total mass in protostars at $t_{\rm END}$, because some protostars are located outside the main clumps.

left panel of Fig. 2, radial streams outside the shell, which appear similar to those found in RCW 120, are developed in *Run 1* after ∼ 1 Myr. These streams are due to the overall gravitational collapse of the molecular cloud; given a non-uniform initial density distributions, the formation of filaments during gravitational collapse is inevitable (Walch et al. 2011). We therefore suggest that the observed radial filaments could have formed as a result of gravitational collapse, independent of ionization feedback.

We are unable to identify pronounced pillar-like structures at the resolution (19.2”) of our synthetic 870 μm images. The SPH mass distribution does show some small pillars and EGGs close to the northwest hole, but in general pillars are not a prominent feature of HII regions expanding into clouds with fractal dimension $\mathcal{D} = 2.4$, because – for this fractal dimension – large-scale density fluctuations dominate the cloud structure.

3.3. Synthetic observations

In a post-processing step we map the SPH density distribution onto a three-dimensional grid, using kernel-weighted interpolation. We choose the grid resolution to be equal to the spatial resolution of 19.2” (Deharveng et al. 2009), achieved when observing RCW 120 with APEX-LABOCA at 870 μm. Assuming a constant gas-to-dust ratio of 100, this immediately gives the dust density distribution from the SPH simulation. The only modification to this rule is that we assume dust to be destroyed at gas temperatures higher than 1200 K,[2] and therefore the dust density is set to a small offset value in these cells; the offset value is 10^{-3} times the minimum dust density in the rest of the computational domain. We only take into account silicate dust grains, on the assumption that these dominate the opacity at 870 μm. We use the standard opacity table for this species given by Draine & Lee (1984).

Using the gridded density distribution, we model the transport of continuum radiation against dust opacity using RADMC-3D[3] (version 0.25; Dullemond, in prep.). In the first step RADMC-3D performs a *thermal* Monte Carlo (MC) radiative transfer simulation to determine the equilibrium dust temperature distribution. The MC method is based on the method of Bjorkman & Wood (2001), but includes various improvements, for instance the continuous absorption method of Lucy (1999). The total luminosity of all sources within the computational domain is distributed amongst $N_{\rm PHOT} = 10 \times 10^6$ photon packages, and $N_{\rm SCAT} = 5 \times 10^6$ photon packages are used to compute scattering events. In one set of radiative transfer calculations we only invoke radiation from the central ionizing star; henceforth we refer to these calculations as *ionizing source only*. In addition, we perform radiative transfer calculations in which radiation from the newly-formed protostars is also included.[4]; henceforth we refer to these calculations as *secondary sources included*, and distinguish quantities derived from these calculations with a superscript $\star$.

---

[2] Temperatures higher than 1200 K are exclusively found within the HII region. Nevertheless, we tested our results against the dust destruction temperature. Increasing it to 1600 K did not show any effect.

[3] http://www.ita.uni-heidelberg.de/ dullemond/software/radmc-

In the second step, RADMC-3D computes isophotal maps at 870 μm, using ray tracing. Figure 4 shows the resulting isophotal maps of our simulations, as seen in their (x, y)-projection. The outer white contour marks the 0.1 Jy/beam cut-off value, which we use to define the total mass of the shell. The inner white contour marks the 0.5 Jy/beam value, which we use to define the masses of the clumps. With radiation from the ionizing source only (top row of Fig. 4), the total flux an observer at 1.34 kpc would receive at 870 μm is $F_{870}^{\rm tot} = 312$ Jy for *Run 1* and $F_{870}^{\rm tot} = 535$ Jy for *Run 2*. If radiation from the secondary sources is included (bottom row of Fig. 4) the resulting total fluxes are significantly higher: $F_{870}^{\rm tot} = 500$ Jy for *Run 1* and $F_{870}^{\rm tot} = 760$ Jy for *Run 2*. The fluxes are higher in the second case, because most of the newly formed protostars are located in or near the clumps.

Qualitatively, the synthetic isophotal maps of our simulations are very similar to the 870 μm observations of RCW 120. In the following, we compare synthetic and observed images in greater detail in order to assess the SPH simulation, but also to evaluate the uncertainty of the mass estimates for clumps in the shell of RCW 120.

We use the 0.5 Jy/beam contour to define clumps within the shell. In particular, we identify the 3 most massive clumps, which we label C1, C2, C3, and focus our analysis on their properties. The total mass and number of sinks located within each clump are listed in Table 1. The mass in gas and dust in the shells and in the individual clumps are listed in Table 2, which we describe more thoroughly in the next section.

4. Discussion

4.1. Clump masses

In order to compare the simulations with observations of RCW 120, we adopt the same technique as in Deharveng et al. (2009) to calculate the masses of the shells and of the individual clumps,

$$M_{870} = 100 \frac{F_{870} D^2}{\kappa_{870} B_{870}(T_{\rm DUST})} \,. \qquad (5)$$

Here D is the distance of the source ($D = 1.34\,{\rm kpc}$ for RCW 120), $\kappa_{870} = 1.8\,{\rm cm^2 g^{-1}}$ (Ossenkopf & Henning 1994) is the dust opacity per unit mass at 870 μm, and $B_{870}(T_{\rm DUST})$ is the Planck function at 870 micron for dust temperature $T_{\rm DUST}$. We adopt $T_{\rm DUST} = 30\,{\rm K}$, since we do not allow the gas to cool below this temperature in the simulations. A constant gas-to-dust ratio of 100 has been assumed.

In Figure 5 we show the mass distribution derived from the isophotal maps using Eq. 5. For reference we overplot the 0.1 Jy/beam and 0.5 Jy/beam contours from Fig. 4, which define – respectively – the shell and the most massive clumps. For *Run 1* we calculate a total shell mass of $1818\,{\rm M_\odot}$ with radiation from the ionizing source only, and $2928\,{\rm M_\odot}$ with radiation from secondary sources included. Both of these estimates are similar to the shell mass of $1,100\,{\rm M_\odot}$ found in RCW 120 with $T_{\rm DUST} = 30\,{\rm K}$. For *Run 2* the corresponding shell masses are $3013\,{\rm M_\odot}$ and $4420\,{\rm M_\odot}$.

4.2. Massive clumps without C&C

We divide the shells up into clumps using the 0.5 Jy/beam contour on the synthetic isophotal

---

3d

[4] The luminosity of the sink sources is calculated according to their mass, assuming that they are main-sequence stars; this probably results in a significant underestimate of their luminosities.

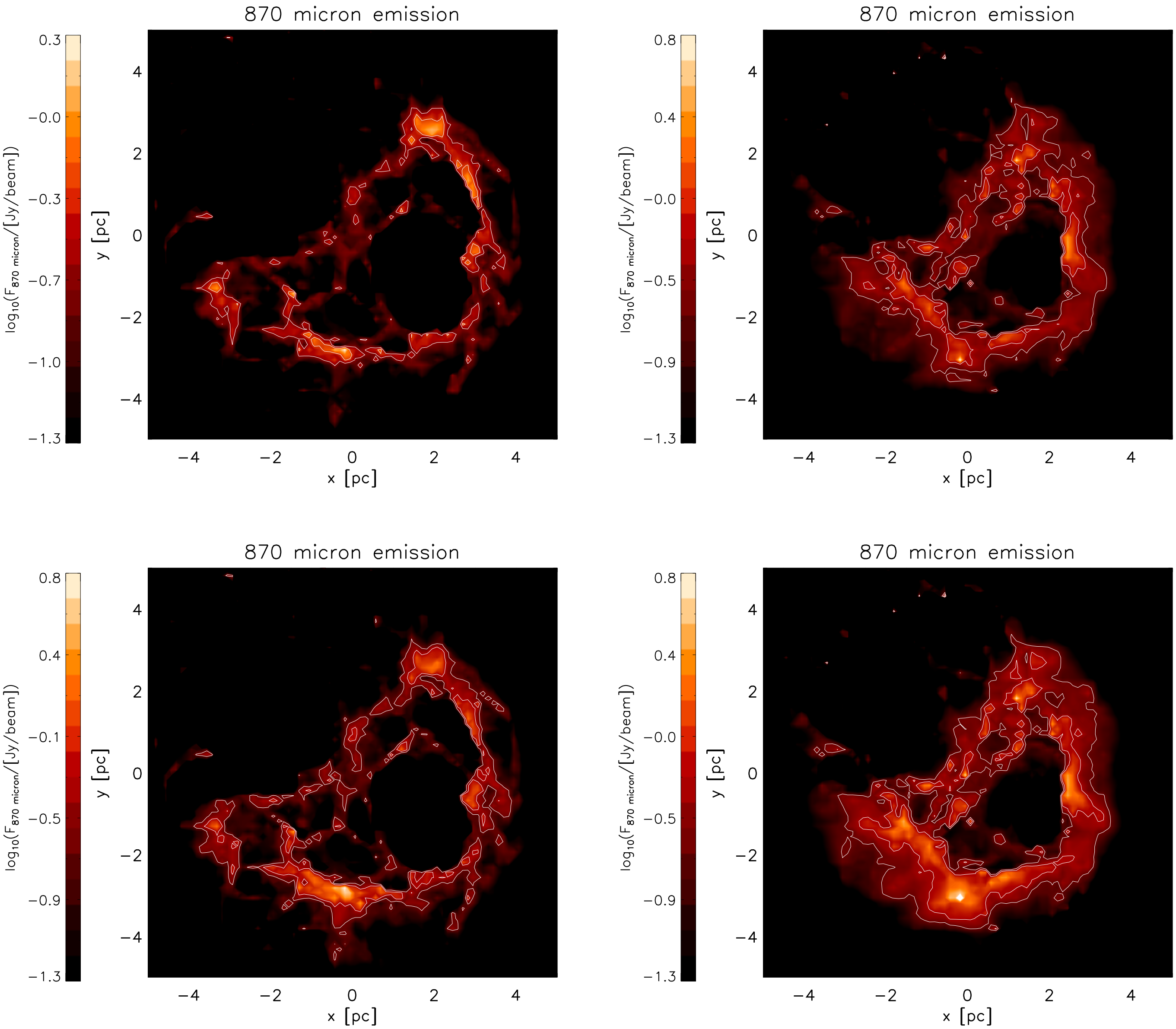

Fig. 4.— 870 micron emission calculated using RADMC-3D. The left column shows the images for Run 1, and the right column for Run 2. The top row shows the images obtained with radiation from the ionizing source only, whereas the bottom row shows the images obtained with radiation from secondary sources included. The white contours are set to fluxes of 0.1 Jy/beam and 0.5 Jy/beam in all images.

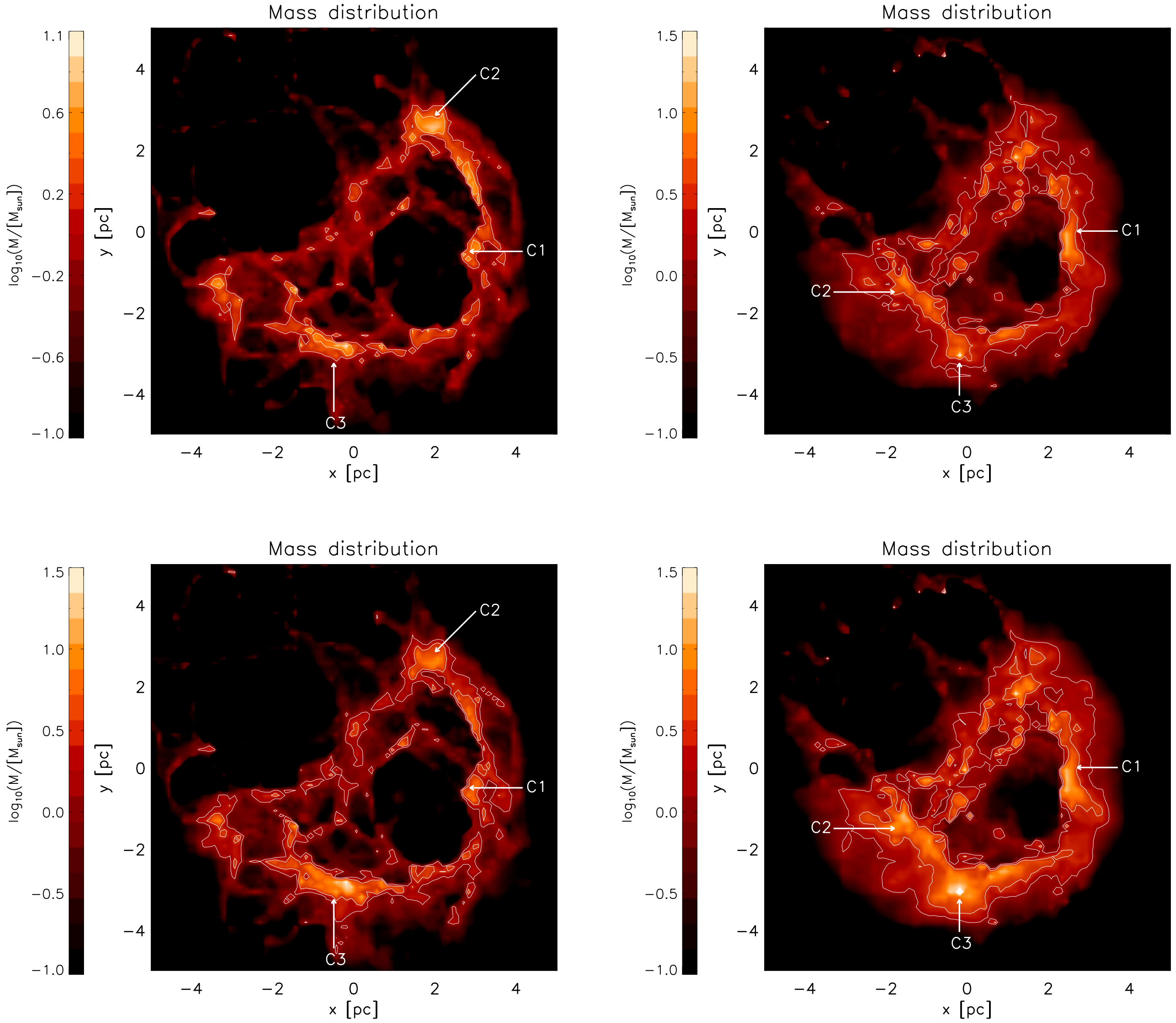

Fig. 5.— Mass distribution derived from the thermal dust emission at 870 μm shown in Fig. 4. For comparison we overlay contours marking 0.1 Jy/beam and 0.5 Jy/beam from Fig. 4. As in Fig. 4, the top row has been calculated with radiation from the ionizing source only, and the bottom row with radiation from secondary sources included. The three largest clumps, which are discussed in the text, are marked with C1, C2, and C3.

maps. These clumps typically have masses between a few and a few hundred $\mathrm{M}_\odot$, depending on the initial cloud density and density PDF. In Fig. 5 we identify the three main clumps formed within each shell and list their properties in Table 2. All these clumps are sufficiently massive to possibly spawn massive protostars.

The clumps are nicely aligned with the forming dense shell and the ionization front. However, our simulations clearly show that the formation of separate clumps in these simulations is not due to C&C. At no time do we observe the formation of a coherent shell, which grows to become gravitationally unstable and then undergoes fragmentation. The formation of clumps simply reflects the clumpiness of the underlying initial molecular cloud structure. Density variations are naturally enhanced by the ionizing radiation, which penetrates low-density regions much more easily than high-density regions. The consequent heating of the low-density regions increases their pressure, and this acts both to disperse the low-density gas, and to compress the remaining high-density clumps. The main clumps in Fig. 5 can clearly be related to structures in the initial column density profile in Fig. 2.

The masses estimated for the three main clumps are strongly dependent on whether the radiative transfer modeling includes the radiation from secondary sources or not (see Table 2 and section 4.3). The variations can be as high as a factor of 8, as is the case for C3 in *Run 1*, for which the estimated mass increases from $61\,\mathrm{M}_\odot$ to $493\,\mathrm{M}_\odot$ when the radiation from secondary sources is included. This is because the extra heating from newly-formed protostars makes the dust in their vicinity hotter, and therefore more material falls within the 0.5 Jy/beam threshold.

4.3. How reliable is the mass distribution obtained from 870 μm fluxes?

In this section we compare how well the actual mass distribution in the simulations is recovered by applying Eq. 5 to the synthetic isophotal maps at 870 μm. This comparison can provide useful insights into the reliability of clump mass estimates from observational data.

We define four masses, which are listed in Table 2. M_{870} is the mass obtained using Eq. 5 on synthetic isophotal maps calculated with radiation from the ionizing source only, and $M^\star_{870}$ is the mass obtained using Eq. 5 on synthetic 870 μm isophotal maps calculated with secondary sources included. Likewise, $M_{\rm TRUE}$ is the actual mass falling within a shell or clump on synthetic 870 μm isophotal maps calculated with radiation from the ionizing source only, whilst $M^\star_{\rm TRUE}$ is the corresponding quantity when radiation from secondary sources is included in the radiation transfer modeling. $M_{\rm TRUE}$ and $M^\star_{\rm TRUE}$ are obtained by integrating the surface density of SPH particles over the area covered by the shell or clump (i.e. the area inside the 0.1 Jy/beam and 0.5 Jy/beam contours, respectively).

The resulting fractional errors,

$$\epsilon \;=\; \frac{|M_{870}-M_{\rm TRUE}|}{M_{\rm TRUE}}\,, \tag{6}$$

and

$$\epsilon^\star \;=\; \frac{|M^\star_{870}-M^\star_{\rm TRUE}|}{M^\star_{\rm TRUE}}\,, \tag{7}$$

are shown in Fig. 6. The shell masses obtained using Eq. 5 on synthetic 870 μm isophotal maps are always lower than the actual mass, typically by a factor $\lesssim 2$, irrespective of whether the radiation from secondary sources is included or not. The masses of individual clumps obtained using Eq. 5 on synthetic 870 μm isophotal maps are sometimes higher and sometimes lower than the true mass; for massive clumps ($> 100\,\mathrm{M}_\odot$) the fractional error is always less than two, but for lower-mass clumps it can be very large, and such masses should probably not be trusted.

In general, masses obtained using Eq. 5 on synthetic 870 μm isophotal maps calculated with radiation from secondary sources are more accurate. However, we note that the inclusion of radiation from secondary sources also increases the dust temperature, and this should be taken into account when applying Eq. 5. In particular, for the three clumps identified in *Run 2*, RADMC-3D gives dust temperatures of about 40 K. This causes us to overestimate the clump masses $M^\star_{870}$ by a factor of

$$\frac{B_{870}(40\,\mathrm{K})}{B_{870}(30\,\mathrm{K})} \simeq 1.4\,. \tag{8}$$

ID	$\frac{M_{870}}{\mathrm{M}_\odot}$	$\frac{M^\star_{870}}{\mathrm{M}_\odot}$	$\frac{M_{\rm TRUE}}{\mathrm{M}_\odot}$	$\frac{M^\star_{\rm TRUE}}{\mathrm{M}_\odot}$
Run 1				
Shell	1818	2928	3031	4450
C1	33	91	5.0	23.
C2	75	146	114	262
C3	61	493	32.	336
Run 2				
Shell	3013	4420	6291	6853
C1	193	302	129	228
C2	74	184	114	270
C3	160	783	89	655

Table 2: Column 1 identifies the different structures analysed. Columns 2 and 3 give mass estimates derived from the synthetic 870 μm images which were calculated with radiation from the ionizing source only, M_{870}, and with radiation from secondary sources included, $M^\star_{870}$ (see Fig. 5). Columns 4 and 5 give the true masses, obtained by integrating the SPH column density over the area inside the 0.1Jy/beam contour for shells, and the 0.5Jy/beam contour for the clumps. $M_{\rm TRUE}$ is the mass within these contour levels calculated with radiation from the ionizing star only, whereas $M^\star_{\rm TRUE}$ is the mass within these contour levels calculated with radiation from the secondary sources included. Both, $M_{\rm TRUE}$ and $M^\star_{\rm TRUE}$ account only for the mass of gas and dust and do not include embedded protostars. The mass in sinks is listed in Table 1.

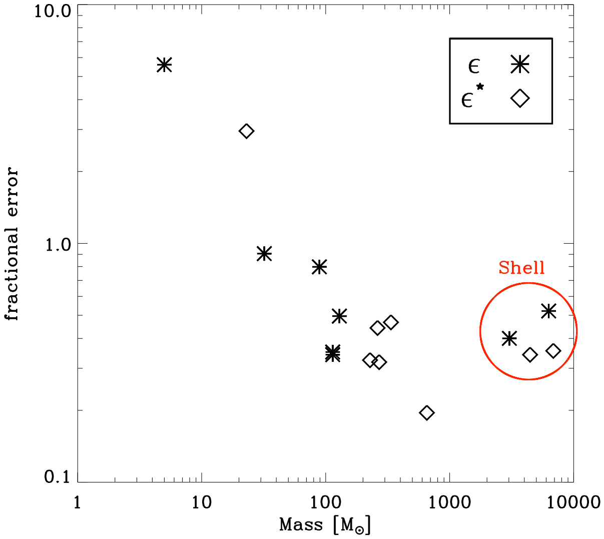

Fig. 6.— Fractional error in the masses estimated for shells and clumps obtained using Eq. 5 on synthetic isophotal maps with and without radiation from newly-formed protostars (see Eqs. 6 and 7).

5. Conclusions

We have performed high resolution SPH simulations of HII regions expanding into fractal molecular clouds, and compared synthetic 870 μm isophotal maps of these simulations (obtained using RADMC-3D) to 870 μm observations of the well-studied, galactic HII region RCW 120.

We conclude that finding massive clumps and sites of high mass star formation within an expanding shell formed around an HII region provides neither proof nor need for the C&C scenario. We suggest that a more accurate description of the triggering mechanism is given by the **E**nhancement of initial **D**ensity substructure and simultaneous **G**lobal **I**mplosion (EDGI) of clumps due to the more efficient heating and dispersal of low-density regions in between denser structures.

The intrinsic clumpiness of the forming dense shell reflects the pre-existing cloud density structure. To first order, regions which later form clumps can already be identified in the initial conditions as areas of enhanced column density.

Overall, we find good agreement (to within a factor of 2) between the actual mass distribution and the mass distribution inferred from thermal dust emission, for shells and clumps having masses greater than $\sim 100\,\mathrm{M}_{\odot}$. In particular, masses obtained using Eq. 5 on synthetic 870 μm isophotal maps always underpredict the overall mass of the the large-scale shell structure, whereas for individual clumps both over- and under-estimates are possible, and usually the result is accurate to within a factor of two.

We note that filamentary streams that are oriented towards the center of the HII region and are located outside of the ionization front are probably not related to, or caused by the HII region itself. We find that such streams form in our simulations due to the overall gravitational collapse of the cloud. Consequently, these dense streams tend to form behind regions where most of the ionizing radiation is trapped by a dense shell of gas and dust. The presence of filamentary streams may hint at the age of the cloud.

S.Walch and A. Whitworth acknowledge the support of the Marie Curie RTN CONSTELLATION. The simulations have been performed on the Cardiff ARCCA Cluster. RW acknowledges support from the Institutional Research Plan AV0Z10030501 of the Academy of Sciences of the Czech Republic and project LC06014 Centre for Theoretical Astrophysics of the Ministry of Education, Youth and Sports of the Czech Republic. DAH acknowledges a Leverhulme Trust Research Project Grant (F/00 118/BJ) and a STFC postdoc. The column density plots were made using the SPLASH visualization code (Price 2007).

REFERENCES

Arthur, S. J., Henney, W. J., Mellema, G., de Colle, F., & Vázquez-Semadeni, E. 2011, MNRAS, 414, 1747

Balsara, D. S. 1995, Journal of Computational Physics, 121, 357

Barnes, J. & Hut, P. 1986, Nature, 324, 446

Bisbas, T. G., Wünsch, R., Whitworth, A. P., & Hubber, D. A. 2009, A&A, 497, 649

Bisbas, T. G., Wünsch, R., Whitworth, A. P., Hubber, D. A., & Walch, S. 2011, ApJ, 736, 142

Bjorkman, J. E. & Wood, K. 2001, ApJ, 554, 615

Churchwell, E., Povich, M. S., Allen, D., Taylor, M. G., Meade, M. R., Babler, B. L., Indebetouw, R., Watson, C., Whitney, B. A., Wolfire, M. G., Bania, T. M., Benjamin, R. A., Clemens, D. P., Cohen, M., Cyganowski, C. J., Jackson, J. M., Kobulnicky, H. A., Mathis, J. S., Mercer, E. P., Stolovy, S. R., Uzpen, B., Watson, D. F., & Wolff, M. J. 2006, ApJ, 649, 759

Dale, J. E., Bonnell, I. A., & Whitworth, A. P. 2007, MNRAS, 375, 1291

Dale, J. E., Wünsch, R., Whitworth, A., & Palouš, J. 2009, MNRAS, 398, 1537

Deharveng, L., Lefloch, B., Zavagno, A., Caplan, J., Whitworth, A. P., Nadeau, D., & Martín, S. 2003, A&A, 408, L25

Deharveng, L., Zavagno, A., Schuller, F., Caplan, J., Pomarès, M., & De Breuck, C. 2009, A&A, 496, 177

Draine, B. T. & Lee, H. M. 1984, ApJ, 285, 89

Elmegreen, B. G. 1994, ApJ, 427, 384

Elmegreen, B. G. & Lada, C. J. 1977, ApJ, 214, 725

Falgarone, E., Phillips, T. G., & Walker, C. K. 1991, ApJ, 378, 186

Federrath, C., Klessen, R. S., & Schmidt, W. 2008, ApJ, 688, L79

—. 2009, ApJ, 692, 364

Gritschneder, M., Burkert, A., Naab, T., & Walch, S. 2010, ApJ, 723, 971

Gritschneder, M., Naab, T., Walch, S., Burkert, A., & Heitsch, F. 2009, ApJ, 694, L26

Hubber, D. A., Batty, C. P., McLeod, A., & Whitworth, A. P. 2011a, A&A, 529, A27+

Hubber, D. A., Walch, S. K., & Whitworth, A. P. 2011b, MNRAS, submitted to MNRAS

Kessel-Deynet, O. & Burkert, A. 2003, MNRAS, 338, 545

Lee, Y. 2004, Journal of Korean Astronomical Society, 37, 137

Lucy, L. B. 1999, A&A, 344, 282

Monaghan, J. J. 1992, ARA&A, 30, 543

Monaghan, J. J. & Gingold, R. A. 1983, Journal of Computational Physics, 52, 374

Ossenkopf, V. & Henning, T. 1994, A&A, 291, 943

Osterbrock, D. E. & Ferland, G. J. 2006, Astrophysics of gaseous nebulae and active galactic nuclei, ed. Osterbrock, D. E. & Ferland, G. J. (University Science Books)

Padoan, P., Jones, B. J. T., & Nordlund, A. P. 1997, ApJ, 474, 730

Padoan, P. & Nordlund, Å. 2002, ApJ, 576, 870

Price, D. J. 2007, PASA, 24, 159

Sánchez, N., Alfaro, E. J., & Pérez, E. 2005, ApJ, 625, 849

Sandford, II, M. T., Whitaker, R. W., & Klein, R. I. 1982, ApJ, 260, 183

Shadmehri, M. & Elmegreen, B. G. 2011, MNRAS, 410, 788

Springel, V., Yoshida, N., & White, S. D. M. 2001, New Astronomy, 6, 79

Stamatellos, D., Whitworth, A. P., & Hubber, D. A. 2011, ApJ, 730, 32

Stutzki, J., Bensch, F., Heithausen, A., Ossenkopf, V., & Zielinsky, M. 1998, A&A, 336, 697

Vogelaar, M. G. R. & Wakker, B. P. 1994, A&A, 291, 557

Walch, S., Whitworth, A. P., & Girichidis, P. 2011, MNRAS, accepted by MNRAS, arXiv:1109.0280

White, G. J., Nelson, R. P., Holland, W. S., Robson, E. I., Greaves, J. S., McCaughrean, M. J., Pilbratt, G. L., Balser, D. S., Oka, T., Sakamoto, S., Hasegawa, T., McCutcheon, W. H., Matthews, H. E., Fridlund, C. V. M., Tothill, N. F. H., Huldtgren, M., & Deane, J. R. 1999, A&A, 342, 233

Whitworth, A. P., Bhattal, A. S., Chapman, S. J., Disney, M. J., & Turner, J. A. 1994a, A&A, 290, 421

—. 1994b, MNRAS, 268, 291

Wünsch, R., Dale, J. E., Palouš, J., & Whitworth, A. P. 2010, MNRAS, 407, 1963

Zavagno, A., Deharveng, L., Comerón, F., Brand, J., Massi, F., Caplan, J., & Russeil, D. 2006, A&A, 446, 171

Zavagno, A., Pomarès, M., Deharveng, L., Hosokawa, T., Russeil, D., & Caplan, J. 2007, A&A, 472, 835

This 2-column preprint was prepared with the AAS LaTeX macros v5.2.